

**FINAL REPORT TO AFOSR**

**APRIL 2005**

**Program Title:** *Development of Artificial Haircell Sensors*

**Principal Investigator:** *Chang Liu, University of Illinois*

*Micro Actuators, Sensors, and Systems Research Group  
Micro and Nanotechnology Laboratory  
The University of Illinois at Urbana-Champaign  
203A Engineering Hall  
1308 Green Street  
Urbana, IL 61801*

*Phone: (217) 333-4051*

*Fax: (217) 244-6375*

*E-mail: [changliu@uiuc.edu](mailto:changliu@uiuc.edu)*

**Co-Principal Investigators:** *Fred Delcomyn, Department of Entomology,  
University of Illinois, Urbana-Champaign  
Sheryl Coombs, Department of Biological Sciences  
Bowling Green University*

**Agreement Number:** *F49620-01-1-0496*

**DISTRIBUTION STATEMENT A**  
Approved for Public Release  
Distribution Unlimited

**20050427 083**

## REPORT DOCUMENTATION PAGE

AFRL-SR-AR-TR-05-

Public reporting burden for this collection of information is estimated to average 1 hour per response, including the time for reviewing instructions, searching the collection of information. Send comments regarding this burden estimate or any other aspect of this collection of information, including suggestions for reducing the burden, to Washington Headquarters Services, Directorate for Information Operations and Reports, 1215 Jefferson Davis Highway, Suite 1204, Arlington, VA 22202-4302, and to the Office of Management and Budget, Paperwork Project, Washington, DC 20503.

0147

1. AGENCY USE ONLY (Leave blank)		2. REPORT DATE	3. REPORT TYPE AND DATES COVERED Final 01 Sept 01- 01 Sept 04
4. TITLE AND SUBTITLE (Bio-Inspired Theme) Development of Artificial Haircell Sensors			5. FUNDING NUMBERS F49620-01-1-0496
6. AUTHOR(S) Liu, Chang			
7. PERFORMING ORGANIZATION NAME(S) AND ADDRESS(ES) The University of Illinois at Urbana-Champaign 801 South Wright Street 109 Coble Hall Champaign, IL 61820-6242			8. PERFORMING ORGANIZATION REPORT NUMBER
9. SPONSORING/MONITORING AGENCY NAME(S) AND ADDRESS(ES) AFOSR/NL 875 North Randolph Street Suite 325, RM 3112 Arlington, VA 22203			10. SPONSORING/MONITORING AGENCY REPORT NUMBER
11. SUPPLEMENTARY NOTES			
12a. DISTRIBUTION AVAILABILITY STATEMENT Approve for Public Release: Distribution Unlimited			12b. DISTRIBUTION CODE
13. ABSTRACT (Maximum 200 words) Biological haircells are highly sensitive and yet robust mechanoreceptors that can respond to an extremely wide variety of physical, fluidical, and chemical stimulus. The variety of animals that use haircell, a simple mechanical transducer, for critical tasks is astonishing. This project aimed to: (1) Learn from the biological systems about haircell sensor design, materials, and performance, and the way multiple sensors are organized; (2) Develop artificial haircell sensors that are inspired by design, materials, and dimensions of biological counterparts using advanced microfabrication strategies; (3) Characterize the performance of artificial haircell sensors and validate the performance of individual sensors and groups of them for flow sensing applications. Apart from the objectives of gaining better performance in terms of combined sensitivity and robustness, the use of bioinspired haircell sensors have other benefits that are important for the military. Sensors are very important for military platforms such as remote wireless sensors and various mobile platforms. However, the cost of developing custom sensors is very high due to the high cost (millions of dollars) and long duration (several years) of sensor development. It is anticipated that the modular sensor concept will significantly reduce the time it takes to develop a certain sensor and to enable low cost development efforts in the future.			
14. SUBJECT TERMS			15. NUMBER OF PAGES 36
			16. PRICE CODE
17. SECURITY CLASSIFICATION OF REPORT	18. SECURITY CLASSIFICATION OF THIS PAGE	19. SECURITY CLASSIFICATION OF ABSTRACT	20. LIMITATION OF ABSTRACT

## **Table of Contents**

<b>Abstract.....</b>	<b>3</b>
<b>Accomplishments .....</b>	<b>4</b>
<b>Area 1: Development of Artificial Haircell Sensors.....</b>	<b>4</b>
<b>Area 2: Development of Artificial Lateral Line Flow Sensing System .....</b>	<b>8</b>
<b>Area 3: Characterization of Artificial Lateral Line Sensing System .....</b>	<b>17</b>
<b>Area 4: New Materials for Bioinspired Sensors.....</b>	<b>27</b>
<b>Summary and Conclusions.....</b>	<b>31</b>
<b>Personnel Supported.....</b>	<b>32</b>
<b>Publications .....</b>	<b>33</b>
<b>Conference Proceedings .....</b>	<b>Error! Bookmark not defined.</b>
<b>New Discoveries, inventions, or patent disclosures.....</b>	<b>34</b>
<b>Honors/Awards .....</b>	<b>34</b>
<b>References.....</b>	<b>35</b>

## Abstract

Biological haircells are highly sensitive and yet robust mechanoreceptors that can respond to an extremely wide variety of physical, fluidical, and chemical stimulus. The variety of animals that use haircell, a simple mechanical transducer, for critical tasks is astonishing. This projected aimed to:

- (1) Learn from the biological systems about haircell sensor design, materials, and performance, and the way multiple sensors are organized;
- (2) Develop artificial haircell sensors that are inspired by design, materials, and dimensions of biological counterparts using advanced microfabrication strategies;
- (3) Characterize the performance of artificial haircell sensors and validate the performance of individual sensors and groups of them for flow sensing applications.

Apart from the objectives of gaining better performance in terms of combined sensitivity and robustness, the use of bioinspired haircell sensors have other benefits that are important for the military. Sensors are very important for military platforms such as remote wireless sensors and various mobile platforms. However, the cost of developing custom sensors is very high due to the high cost (millions of dollars) and long duration (several years) of sensor development. It is anticipated that the modular sensor concept will significantly reduce the time it takes to develop a certain sensor and to enable low cost development efforts in the future.

During the past 3.5 years, an interdisciplinary research team, lead by Prof. Chang Liu of the University of Illinois, has tackled scientific and engineering issues that pertain to the stated goals. Dr. Liu worked with biologist, including entomologist Prof. Fred Delcomyn (who studies individual haircell response) and fish biologist Prof. Sheryl Coombs (who studies response of a group of haircells connected by neurons).

Significant progress has been made in the engineering front. Three generations of haircell sensors have been made, each with increasing degree of robustness. The third generation device was entirely made of polymer materials above the substrate surface. The sensor performance has been characterized experimentally as well as modeled analytically. These three generations of haircells can perform flow sensing tasks with sufficient sensitivity. The biggest accomplishment on the engineering front is that the researchers have established a line of fabrication method and design expertise for making haircells that are viable for larger scale prototyping and industrial implementation in the future.

The researchers have studied biological systems with the objective of extracting valuable design lessons for engineering sensors. This type of engineering-driven study of biological haircells has rarely been done in the past. As such, work performed in the past three years is extremely valuable and provided many design insights for engineering. A core team is established, permitting future efforts to be conducted at a greater scale and deeper level.

Overall, the research team accomplished the tasks set out in the proposal.

## **Objective**

This project involved in developing biomimetic sensors with their architectures inspired by the biological haircells, a sensing element commonly found in many species of the biological world. The haircells are used for hearing and balance (e.g. human inner ear), for flow sensors (e.g. cerci organs of certain insects), for contact sensing (skin), and for imaging of fluid fields (e.g. lateral line of fish). The main focus of this project was designing the basic artificial haircell unit, developing a successful fabrication process to realize sensitive and yet reliable sensors, and subsequently prove the basic functionalities of such sensors.

The artificial haircell sensor concept is developed to realize modular integrated sensors, or application specific integrated sensors (ASIS). Sensors are very important for military platforms such as remote wireless sensors and various mobile platforms. However, the cost of the sensors, especially ones with custom specifications, is very high. It is anticipated that the modular sensor concept will reduce the time it takes to develop a certain sensor and to enable low cost development efforts in the future. This is expected to greatly enhance the military's ability to sense environmental variables.

## **Accomplishments**

Major accomplishments are summarized in the following according to several major areas: (1) development of artificial haircell sensors; (2) development of artificial lateral line sensors; (3) characterization of artificial lateral line sensors; and (4) new materials for bioinspired sensors.

### ***Area 1: Development of Artificial Haircell Sensors***

In the first year of the program, Dr. Liu's group successfully developed a novel microfabrication process combining bulk silicon micromachining and three-dimensional assembly to realize an artificial haircell array based on single-crystal silicon as shown in Figure 1. The vertical cilium was developed using plastic deformation magnetic assembly method, which is very efficient and capable of generating arrayed devices over large wafer surface areas as shown in Figure 2. Force applied horizontally to the cilium – including fluid flow, touch, and vibration – created torque acting on the vertical cilium. The torque translated to the horizontal cantilever and generated stress at the location of in-plane strain sensors. The amount of applied force could be inferred from the change of resistance.

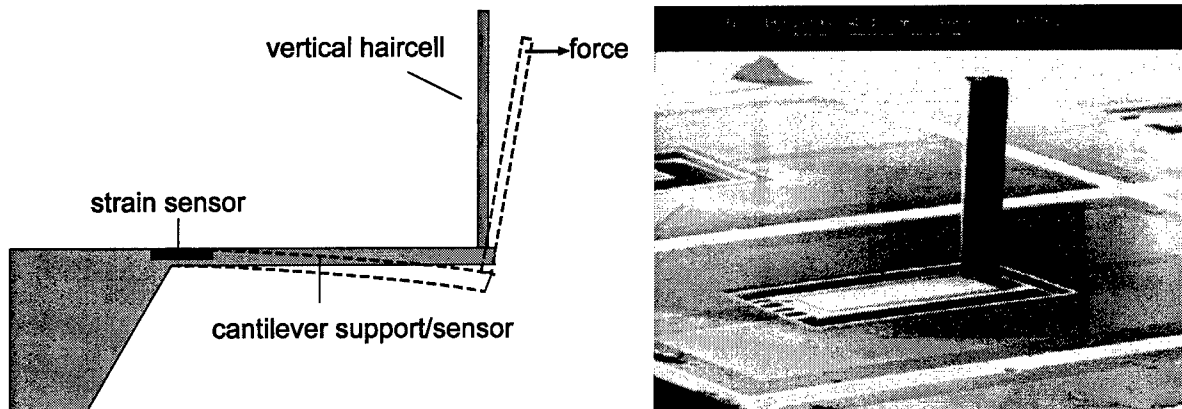


**Figure 1: Schematic diagram and an SEM of silicon based artificial haircell developed in the first year of the program.**

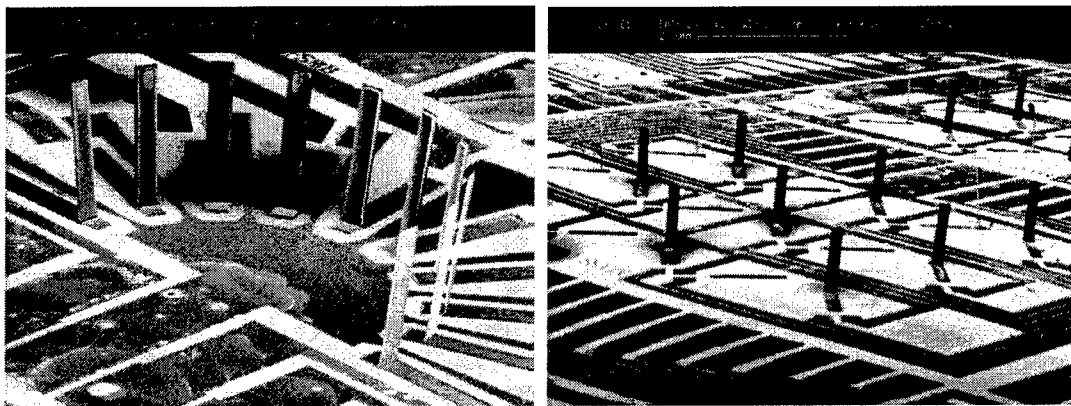


**Figure 2: SEM of arrays of artificial haircell sensors with distributed angular positions.**

In the second year, Dr. Liu's group had further advanced the state-of-the-art by realizing an artificial haircell sensor based on photosensitive polyimide. Polymer material is of lower cost and greater durability than silicon material. The polymer based artificial haircell, schematically diagrammed in Fig3a, is composed of a vertical beam (artificial cilium) rigidly attached to the substrate. Attached at the base of the beam, between the cilium and the substrate, is a strain gauge. The strain gauge is comprised of a thin film Nichrome (NiCr) resistor on a thicker polyimide backing that runs the length of the cilium.

When an external force was applied to the vertical beam, either through direct contact with another object (functioning as a tactile sensor) or by the drag force from fluid flow (flow sensing), the beam will deflect and cause the strain gauge to stretch or compress. The strain gauge region was treated as being rigidly attached to the substrate, while the cilium is free. The magnitude of the induced strain was greatest at the base, where the strain gauge was located.

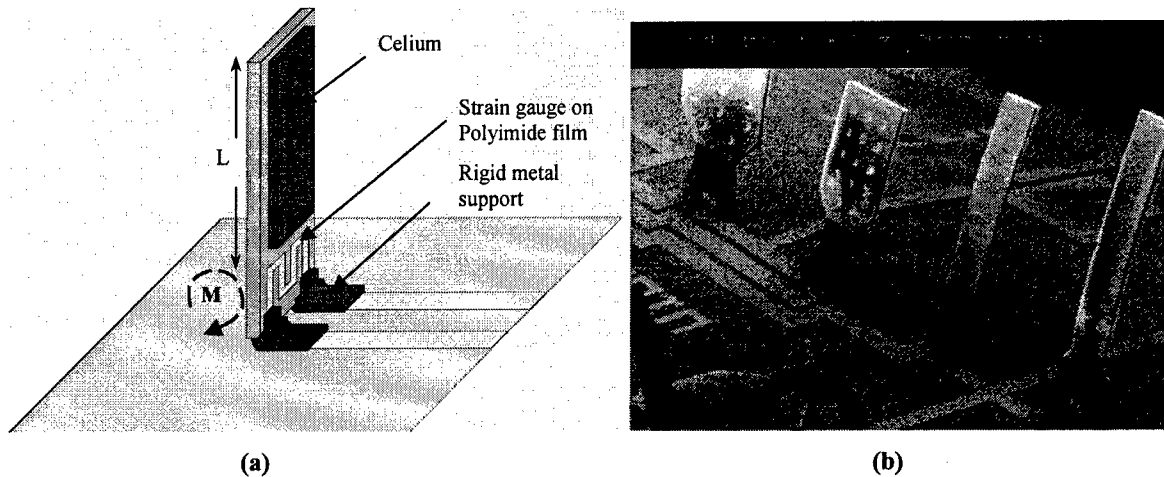


Figure 3: Schematic diagram and an SEM of a polyimide artificial haircell.

All polymer micro sensors are desired in certain cases, such as flow sensing. Previous work with artificial haircell (AHC) MEMS flow sensors [1] and elastomer patterning [2] has been combined to realize a wholly polymer flow-sensing structure. Newly developed fabrication processes (Figure 4) combined unorthodox techniques (e.g., lost wax sacrificial processing) to realize tall (3 mm) and high aspect ratio vertical polyurethane integrated with precision-patterned elastomer force sensitive resistors (FSRs). Although conductive rubber FSRs have been used in robotics for years [3] and commercial FSR products exist, these sensing elements have not been previously photolithographically patterned (see Figure 5).

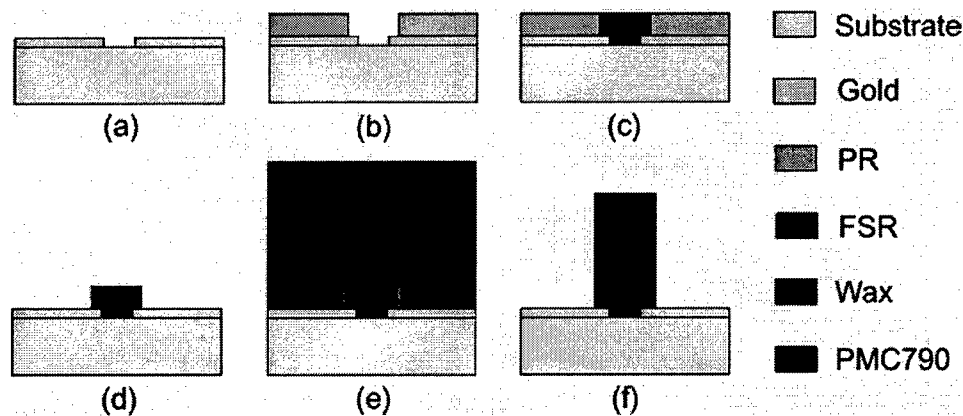


Figure 4: Fabrication flow: a) Deposition of gold wiring; b) patterning of photoresist mold; c) filling mold with FSR; d) removal of mold; e) alignment of urethane hair in wax mold; f) removal of wax mold. A lost-wax sacrificial process is developed and used.

Dr. Liu's group conducted a detailed study investigating the properties and performance of 2-part polyurethane rubber elastomers as materials for MEMS. So far, polydimethylsiloxane (PDMS) is the most commonly used elastomer in MEMS, especially microfluidics. But PDMS has limited mechanical properties. Polyurethanes are stiffer than PDMS and offer better thermal degradation and tear resistance. His group also demonstrated new designs and processes for polyurethane polymers with a robust, all-polymer artificial haircell sensor.

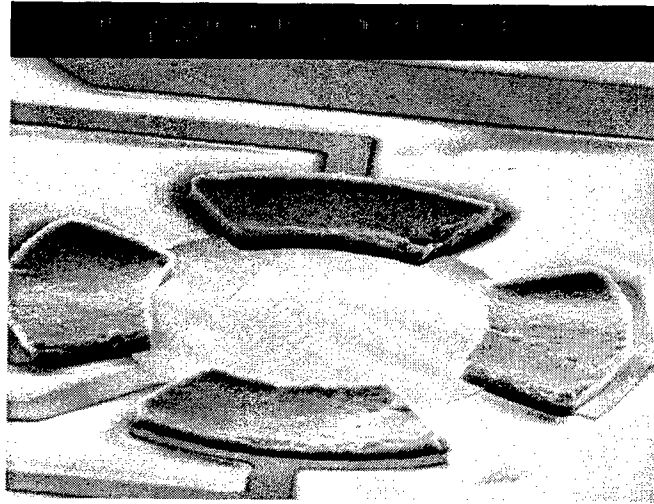
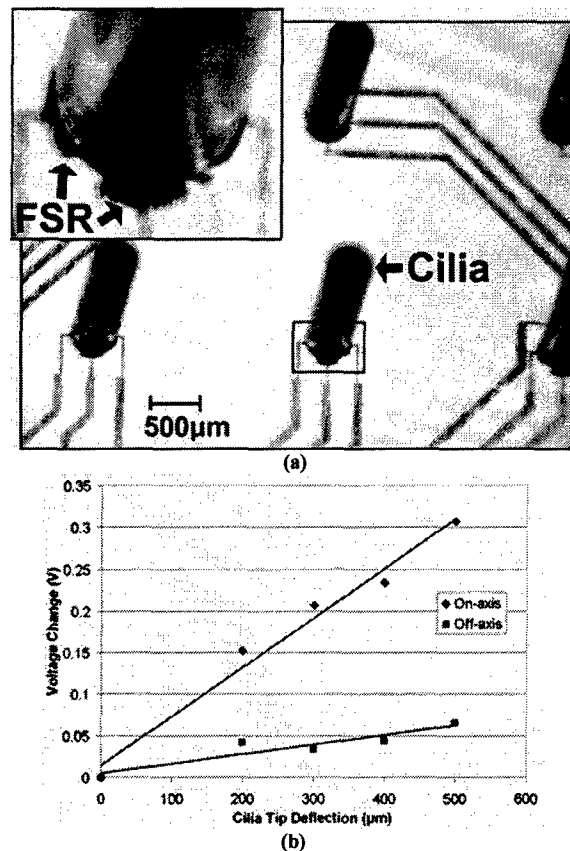


Figure 5: SEM of FSR and wiring bridge layout.

The group established a new material for the MEMS field. Polyurethanes represent a group of elastomeric polymers with wide-ranging properties. Like PDMS, polyurethanes offer low cost and mold process capability. Characterization of a full set of material and processing-related properties (e.g., surface treatment, tensile modulus, adhesive strength, chemical resistance, and thermal degradation) has been performed based on two polyurethane rubbers (PMC121 and PMC790 [4]). *Thermal degradation* testing showed that polyurethanes withstand long-term exposure to temperatures commonly encountered in MEMS processing, with weight loss greater than 1% beginning at 125°C. Tensile testing showed that the modulus of PMC121 polyurethane (453 kPa) is close to that of PDMS (750 kPa for Sylgard-184), while PMC790 is an order of magnitude *stiffer* (19.1 MPa). In addition, the *elongation at break* of both polyurethanes is well over 200% strain and both exhibit notch-blunting behavior while PDMS will readily crack.

The principle of operation of the all-polymer sensor is discussed below. The carbon-filled urethane FSRs arranged in a pair of half bridges can determine x and y-axis deflection of the 3mm tall cilia (Figure 6a) with on and off axis performance as shown in Figure 6b. On-axis is the response from x-axis FSRs to x-deflection; off-axis is the response from x-axis FSRs to y-deflection and vice versa. Tip deflection sensitivity is increased 20-fold over earlier work (245ppm/ $\mu\text{m}$  vs. 12.3ppm/ $\mu\text{m}$ ). The current prototype designs do not exhibit perfect off-axis insensitivity due to non-linear behavior of the FSRs and non-uniformity in FSR baseline resistance. The polyurethane hairs can be repeatedly bent by 90°.





**Figure 6: a) Photo of cilia flow sensor array and associated wiring. b) Plot of average on and off-axis response of the presented cilia flow sensor. On and off axis sensitivities are  $590 \mu\text{V}/\mu\text{m}$  and  $115 \mu\text{V}/\mu\text{m}$  respectively when the bridges are excited by  $\pm 3\text{VDC}$ .**

### *Area 2: Development of Artificial Lateral Line Flow Sensing System*

Biological haircell sensors not only offer highly efficient sensing, but also high performance signal processing and sensor networking as well. Signal processing of artificial haircell sensor involves analog to digital conversion and amplification. In biological haircell, these electronics functionalities are achieved with a single neuron. Even with today's advanced microelectronics circuit technology, the signal processing circuitry still occupies much greater footprint than a neuron. Although it is difficult to probe single neuron functionality, we examine the neuron response to mechanical stimulations to identify features of biological sensor design and networking.

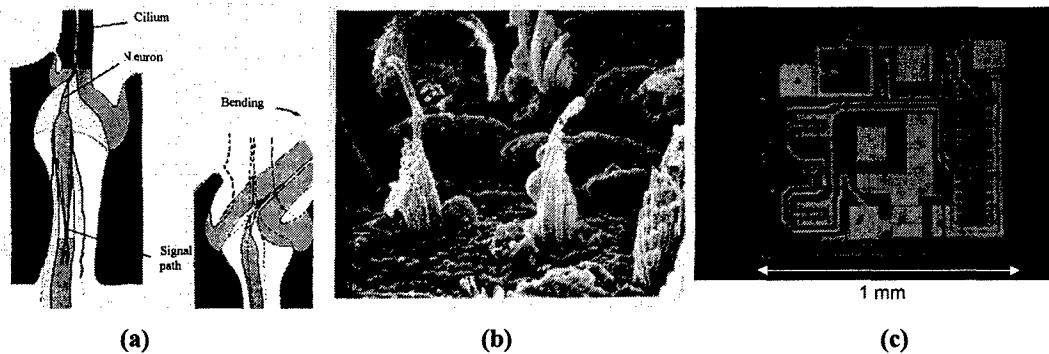


**Figure 7: (a) Schematic diagram of a biological haircell. (b) SEM micrograph of an array of haircell illustrating the high density of integration possible in biology. (3) A state-of-the-art integrated circuit with A/D conversion and amplification functionalities would take a much greater footprint.**

The second generation artificial haircell sensor has been combined with hotwire anemometers to form a sensor pixel, which is directly integrated on top of semiconductor integrated circuit substrates with existing signal processing units. In fact, the hot wire anemometer offers better sensitivity than the haircell sensors at this stage and was used primarily for flow sensing and visualization. The hot wire sensors are described below.

In the past, efforts have been made to apply various micromachining processes to realize HWA for measuring airflow with smaller dimensions, better uniformity, and faster time response. One strategy is to use the bulk-micromachining technique to produce freestanding cantilever structures [5, 6]. Another group undercut a polysilicon hot-wire with wet etching so the hot-wire is suspended over a cavity for better thermal insulation [7]. However, the consumption of the silicon substrate in bulk-micromachining increased the difficulty for integration with electronics circuits.

Dr. Liu's group monolithically integrated the out-of-plane flow sensor on a silicon substrate with pre-existing circuitry. The sensors were fabricated on top of commercial JFET quad operational amplifier (LF347) wafer made by National Semiconductor. Each hot-wire was connected in a feedback bridge circuit to a separate amplifier die to maintain overhead ( $1-R/R_0$ ) of 0.25. The sensors are repeated on each die across the array.

The fabrication was as follows: First, a 5- $\mu$ m-thick polyimide was spun on to passivate and planarize the circuit and subsequently patterned to expose the metal contacts. This was followed by a series of surface micromachining steps to deposit the aluminum sacrificial layer, polyimide structural layer, nickel hot-wire, gold wiring, and Permalloy flap (Figure 8a). The aluminum sacrificial layer was then removed (Figure 8b) and an external magnetic field was applied to plastically deform the gold hinge and raise hot-wire out of plane (Figure 8c). At the same time, selective electroplating of nickel reinforced the outer two hinges. A picture of a fabricated array is shown in Figure 9. The dashed line shows the size of a single die. Two types of sensors were fabricated in the same process, the hot-wire anemometer and an artificial hair cell. Each set of sensors occupies an individual die separated 2.3 mm apart.

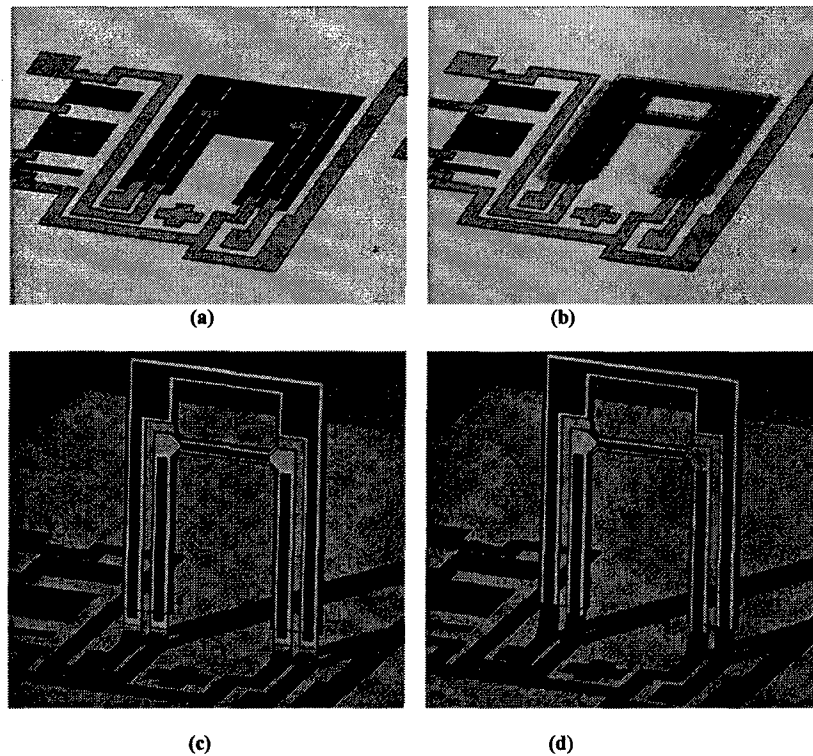


**Figure 8: Fabrication process.** a) Aluminum sacrificial layer is evaporated followed by the spin-on of photodefineable polyimide. Nickel hot-wire and gold wiring is deposited and patterned using lift-off, followed by the electroplating of Permalloy. b) Aluminum sacrificial layer etching in an alkaline solution. c) Apply external magnetic field to raise the structure out of plane. d) Selective electroplating on the outer hinges to reinforce the structure.

The response of several hot-wire to airflow is shown in Figure 10. The voltage swing is about 100mV over a 20m/s flow speed. With the calibration curve we can translate the output voltage swing into airflow. Using a standard data acquisition software, we mapped the voltage output of the fabricated hot-wire array for flow imaging. A flow imaging data is shown in Figure 11. At time  $t=0$ , the peak flow is on the right side of the array, and from  $0 < t < 18$  seconds, the fan is swept across the array. The region of high flow speed (represented by color red) is move from the right side to the left side in the image.

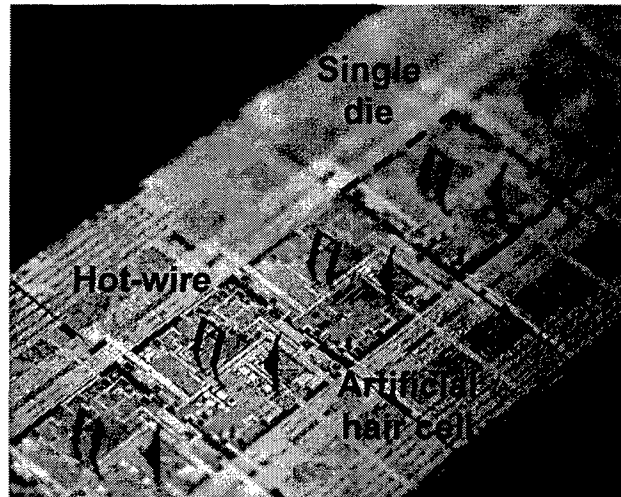


Figure 9: Photograph of the hot-wire array integrated with constant-temperature feedback circuit. Artificial haircell sensors are also integrated on the same substrate, potentially allowing multi-modal, and fully integrated flow sensors.

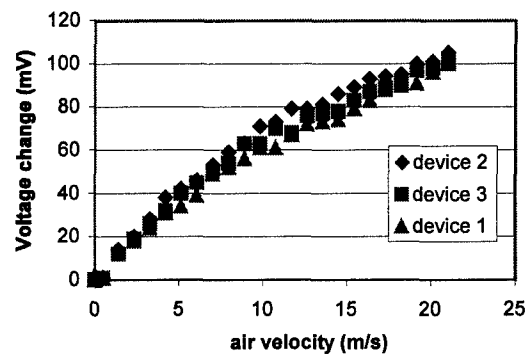


Figure 10: Voltage output of three hot-wire anemometer as a function of air velocity.

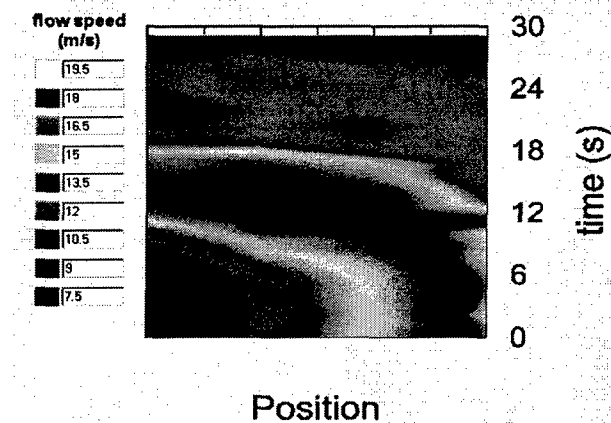


Figure 11: Contour plot of a captured flow profile using LABVIEW. Flow profile generated by sweeping a DC fan across the hot-wire array. Each velocity data is averaged over 1 second.

In the third year, Dr. Liu's group focused their efforts on two issues:

- 1) Demonstrate functionalities of artificial haircell sensors for flow sensing applications. The group focused on developing flow sensors integrated with on-chip electronics signal processors in order to image flow fields (liquid or air). The flow sensor for liquid sensing is modeled after the fish lateral line system. (The lateral line system is described in more details below).
- 2) Further develop polymer micromachining processes and incorporate new polymer materials such as polyurethane.

### **Background on Lateral Line**

Lateral line system has been known for a long time. A brief historical overview has been summarized here[8]. Originally it was thought to be an organ that secretes mucus. Leydig first described the neuromast in the 1850s. Very soon after, it was discovered that the cupula of the neuromast could be stimulated by water movement. The true function of lateral line as a sense organ was observed by Hover in 1908. He discovered that a blind pike could still react to weak water current, but that behavior disappeared after he selectively removed the lateralis nerve fiber. There was originally some confusion regarding what the lateral line detected, suggesting that the lateral line is an extension of fish's hearing organ to detect sound wave. However, using selective elimination of organs surgically, it has been concluded that lateral line is not used for sound reception. The true function of lateral line is to conduct near-field hydrodynamic imaging, it "enables fishes and amphibians to perceive other moving animals as prey, enemies, or sexual partners, without really touching them." [9]

The lateral line system is comprised of a large array of distinct Neuromast that serve as individual sense organs. The neuromasts themselves are the actual mechanosensory organs that respond to the stimulus. The number of neuromast found in a lateral line system can vary from specie to specie, tens to thousands. These organs can be classified into two categories, depending on how they are packaged. The neuromast found exposed on the surface of the fish are called superficial neuromast, which responds to fluid velocity. They are typically found around the head, the grill, and the trunk of a fish, as represented by the red dot in the fish illustration in Fig. 12. A second type of neuromast are packaged in fluid-filled canals beneath the surface of the skin, these are called canal neuromast. These are represented by the solid blue line. Because the movement of fluid inside the canal is proportional to the derivative of the velocity of fluid outside the canal, they serve as acceleration sensors[10]. A more detailed description of the lateral line system can be found here[9, 11-13].

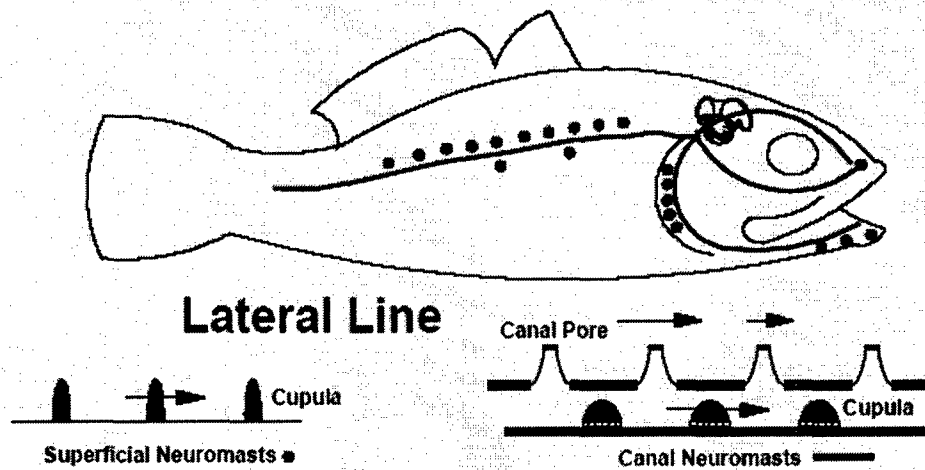


**Figure 12** Illustration of the superficial and canal neuromast and where they may be found in a fish

Upon closer observation, the neuromast themselves are relatively complicated organs made of several components. Each neuromast typically contain tens to hundreds of hair cells, which are individual nerve cells that form the fundamental building block of the octavalateralis system, and are found in all vertebrates. They are inherently displacement detectors that have a preferred orientation to give them directionality. They haircells that populate a neuromast are always arranged in two groups that intermingle with each other but have directly opposite orientation. Each neuromast is innervated by at least 2 afferent nerve fibers, one for each direction. Multiple nerve fibers can connect to the same neuromast. For canal neuromast, a nerve fiber never connects to more than one neuromast. Similarly, for superficial neuromast, a nerve fiber will not connect to neuromast that are in different rows. The extremity of the neuromast is covered by a gelatinous sack called the cupula. The cupula serves to protect the hair cells and to couple motion of the surrounding fluid to haircell deflection. It has a density that is similar to the surrounding fluid, and is driven primarily by viscous force[14, 15]. The cupula displacement is proportional to the velocity of the surrounding fluid.

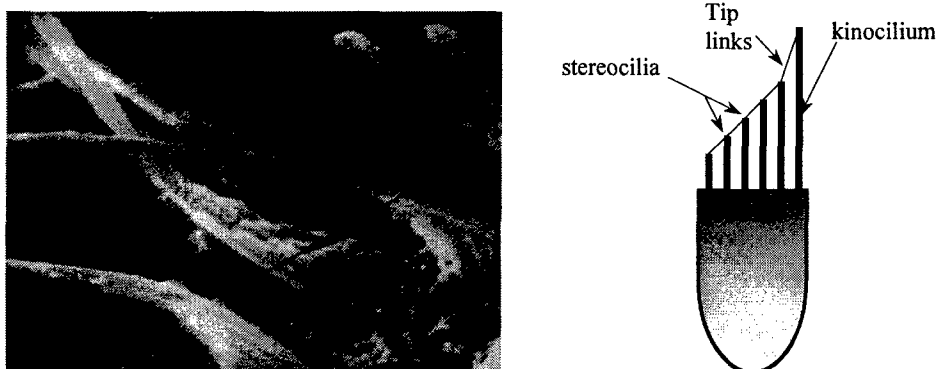


**Figure 13** SEM and schematic of a haircell.

The actual sensory unit found in the octavolateralis system is the haircell. Protruding away from the haircell are bundles of hair called the cilia. They are arranged in order of increasing height, with the shortest cilia at one end, and the tallest one (kinocilium) at the other end, as shown in Fig. 13. The top of the stereocilia are connected by tip links. When the haircell are deformed in the direction towards the kinocilium, the tip link experiences tensile stress, which leads to the opening of the ionic transduction channel into the haircell and increases in the firing rate of the nerve fiber. Deflection in the opposite direction away from the kinocilium leads to the closing of the ionic transduction channel[16]. This understand of haircell transduction is described as the gating-spring model[17]. Haircell is very sensitive and has been estimated to sense motions down to 0.3nm range, below where Brownian motion becomes significant.

The signals from the two opposing direction of haircells are conveyed to the nervous system in separate channels. In canal neuromast, the haircells typically orient along the direction of the canal. Lateral line hair cell differ in dimension across species. Using incident light polarization microscopy, the haircell found in ruff, *Acerina cernua* L, has been visualized *in vivo*[18]. The haircells are pear shaped and 15 $\mu$ m high. The base dimension is about 7~10 $\mu$ m.

#### **Micromachined hot-wire lateral line system**

The design and fabrication of the new type HWA is based on surface micromachining. Micromachining describes the manufacturing process of creating features with critical dimension the  $\mu$ m range. Many, but not all, of the process used are derived from the technologies developed for integrated circuits (IC) manufacturing[19]. Like IC manufacturing, multiple devices can be fabricated on each die, and multiple dies on each wafer. Therefore, hundreds or thousands of HWA can be fabricated simultaneously with good yield and uniformity.

The fabrication process involves surface micromachining, a additive and subtractive process common in microelectromechanical systems (MEMS) to create free-standing cantilevers[20];as well as a three-dimensional assembly process that can raise the cantilevers out of plane. Surface micromachining is used to define the HWA, including a nickel-iron alloy support prong, and a nickel-polymer composite hot-wire sensing element. 3D assembly is used to raise the sensor out of plane, which thermally insulate the hot-wire and allow the sensor to interact with the fluid above the boundary layer. Detailed fabrication and discussion has been presented in detail[1] and will not be discussed in detail here, but it has been demonstrated that large array of the sensor can be fabricated in parallel for flow sensing, and even monolithically integrating with basic signal conditioning and amplifying circuits[21].

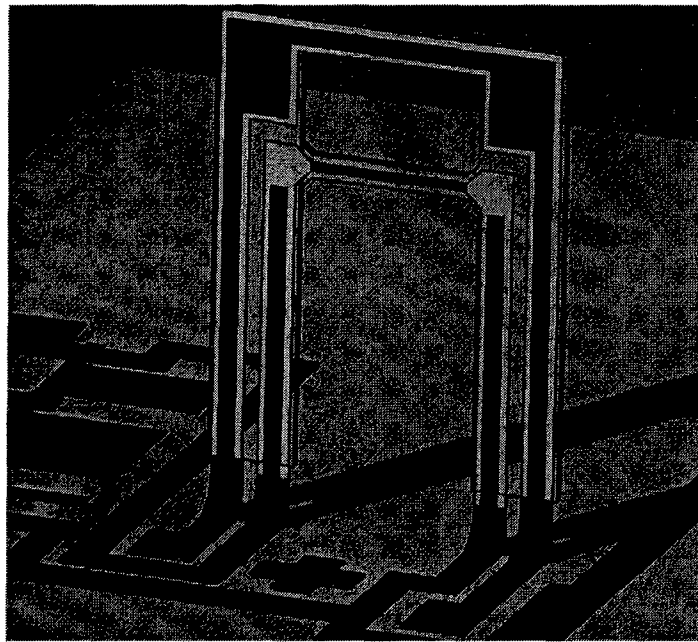


**Figure 14:** Schematic of a surface micromachined, out-of-plane HWA with 200- $\mu\text{m}$ -long by 10- $\mu\text{m}$ -wide hot-wire elevated 400 $\mu\text{m}$  above the substrate.

A schematic of a single micromachined HWA is shown in Figure 12. The hot-wire is different with the conventional ones, it is made of a thin film nickel/polyimide composite. The 100 nm-thick-nickel is deposited by thermal evaporation with an as-deposited sheet resistance of  $1\Omega/\square$ , and has a temperature coefficient of resistance ( $\alpha$ ) of 4100ppm/ $^{\circ}\text{C}$ . The nickel filament is sandwiched by 2 layers of polyimide that serves to provide passivation, structural support, and electrical isolation. This has an advantage of achieving a large electrical resistance due to thin-film metal and reduced conduction end loss due to the low thermal conductivity of polyimide. HWA fabricated in this method can have wire length from as small as 50 to as long as 400 $\mu\text{m}$ , and as tall as 1mm. For the single channel testing presented here, a 200- $\mu\text{m}$ -long hot-wire elevated 1mm high is used. For the array testing, because we want a higher sensitivity, a 400- $\mu\text{m}$ -long hot-wire elevated 600  $\mu\text{m}$  is used.

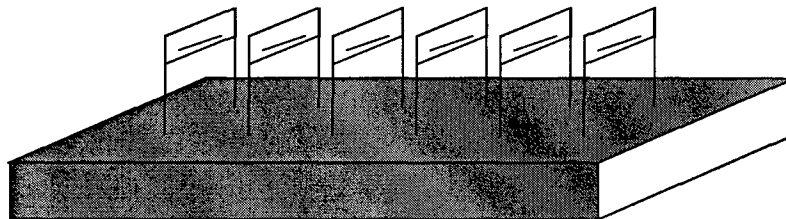


**Figure 15:** Schematic of a fabricated array

In the experiment, an artificial lateral line system was fabricated using micromachined, out-of-plane, HWA to serve as individual neuromast. Each HWA array (die) was made of 16 individual sensors equally spaced 1mm apart. The sensors were fabricated on a 2" silicon wafer that can



hold up to 8 dies. After surface micromachining process, the dies were separated and the HWA was assembled using our custom 3D assembly process. Each array was then packaged and wire-bonded onto a PC board and waterproofed by using a  $2\mu\text{m}$  thick vapor-coated parylene film that waterproof all the exposed wiring and to prevent electrolysis of water at the hot-wire.

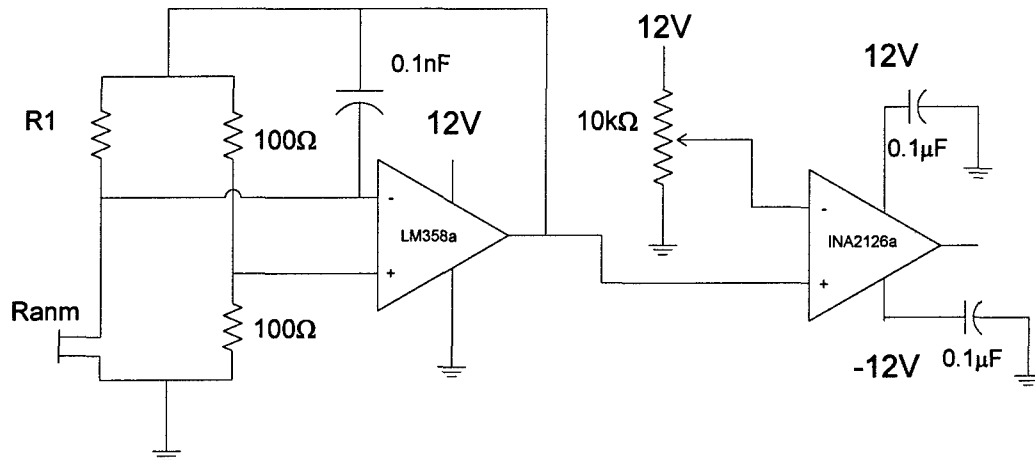


**Figure 16:** Schematic of the signal conditioning circuit for the 16-channel array. The overheat of the HWA ( $R_{\text{anm}}$ ) in the CTA circuit is set by the potentiometer  $R_1$  with the equation  $R_1 = R_{\text{anm}}(1+a_R)$ . The gain of the ina2126 instrumentation amplifier is set to 500.

### Artificial Lateral Line Canal packaging

As noted in earlier discussion, the superficial neuromast response primarily to viscous drag from the difference in velocity between the animal and the surrounding fluid. When the velocity difference is large the output signal superficial neuromast can be swamped with this DC noise and become relatively insensitive to the small ac stimulus. One solution is to follow the example from biology and imbed the sensor in an artificial lateral line canal, which serves as a high-pass filter to attenuate the DC signal. To do that, we add an additional molding step similar to the method we used to create a water channel for volumetric flow rate measurement[21]. A silicone elastomer, polydimethylsiloxane (PDMS), is mixed in a 5:1 ratio and then poured onto a Teflon mold patterned by milling. The PDMS is then cured inside the mold and then separated. Some holes are punched into the PDMS to create the similar pore structure and the PDMS channel is then optically aligned with the HWA array and permanently bonded. The artificial canal is a useful package because it also can protect the out-of-plane HWA from being damaged.

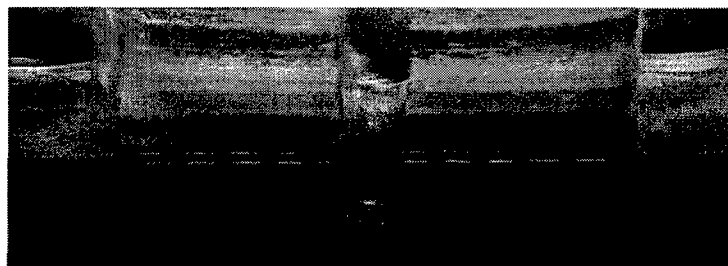


**Figure 17:** Optical micrograph of a HWA enclosed in a PDMS channel that serves as an artificial lateral line canal

### ***Area 3: Characterization of Artificial Lateral Line Sensing System***

For the individual hot-wire measurement, the HWA was interfaced with a modular signal conditioning system from TSI that includes an anemometer module (model 1053B), a decade resistance module (model 1056) to control the overheat ratio, and a power supply module (model 1051-1). The output passes through a Grass Telefactor P55 AC preamplifier, with the band pass filter set between 10 and 300Hz, and a gain of 60dB.

For array measurement, a custom circuit (circuit for a single channel shown in Figure 166) was used for signal conditioning for all 16 channels on the HWA that includes a constant temperature (CT) feedback circuit whose output was sent to an instrumentation amplifier. A trimming potentiometer is used to remove the DC offset before each measurement.

#### **Single channel testing**

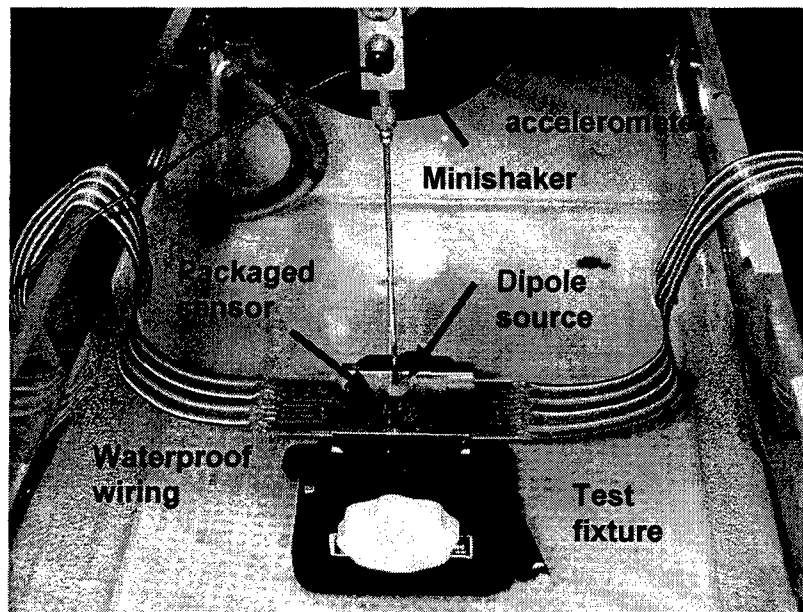


**Figure 18:** Picture of the experimental setup. The minishaker is rigidly attached to the 3-axis linear stage, with one of the axis controlled by a wormgear motor. The  $\frac{1}{4}$ " diameter dipole source, which is submerged in water, is attached to the minishaker through a 12-gauge needle. The accelerometer is attached to the base of the rod. The sensor is mounted on a test fixture that is rigidly attached to the base of the water tank with a suction cup, and is entirely submerged in water.

All testing of the HWA was performed in water. The setup is similar to the hydrophone and neural recording experiment[22]. The experimental setup is shown in Figure 17. A B&K 4010 minishaker was attached to a 3 axis linear stage, with one axis of motion controlled by a worm gear motor. A 3mm diameter sphere was attached to the minishaker through a 12-gauge needle that serves as the dipole source. An accelerometer was attached to the base of the needle to measure the acceleration of the dipole. The packaged HWA was mounted on a test fixture that is rigidly attached to the base of the water tank through a suction cup. Since this is a single sensor channel calibration, the TSI anemometer circuit is used along with the Grass preamplifier. The signal amplitude was measured using the HP 3581 waveform analyzer.

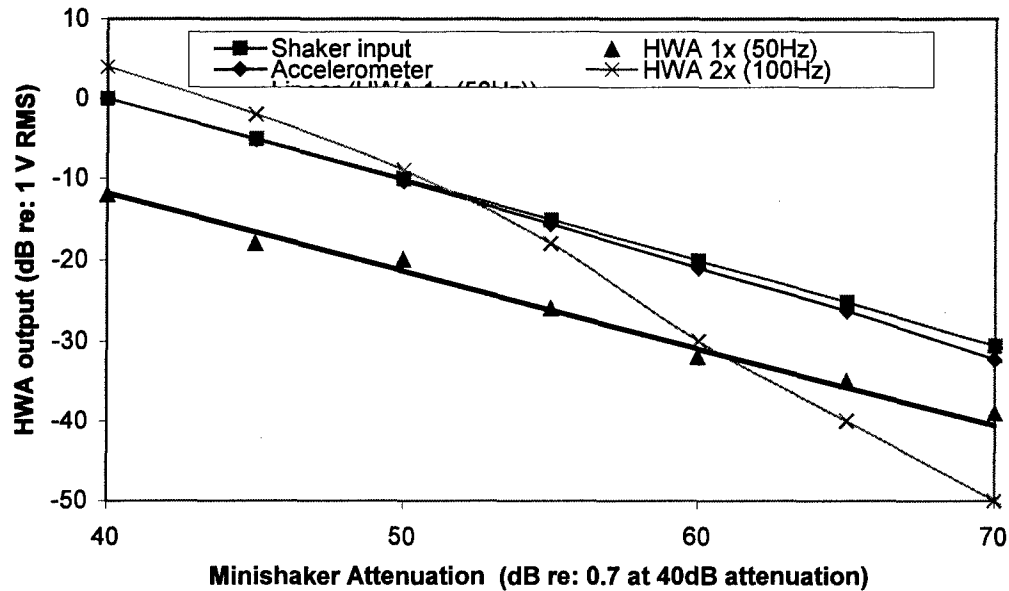
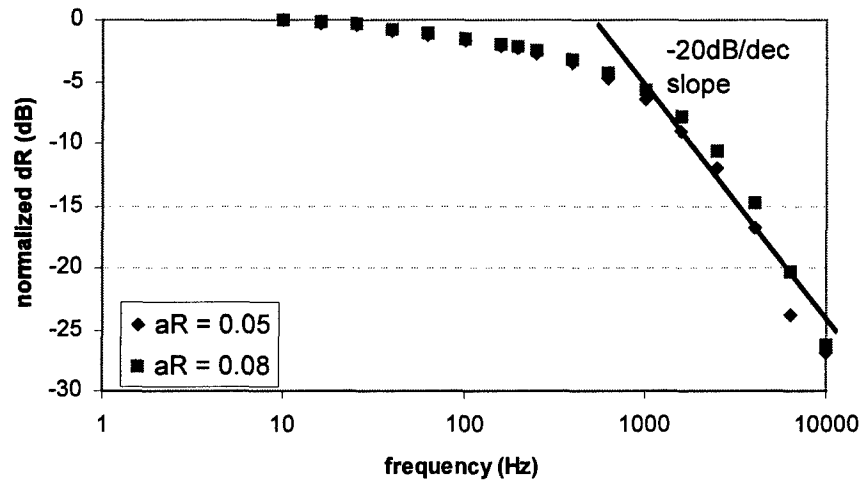


**Figure 19:** Input-Output response of the HWA to shaker attenuation ( $0.7V_{rms}$  to the shaker @40dB). The frequency of the minishaker and the frequency where the amplitude of the HWA output is measured is at 50Hz.

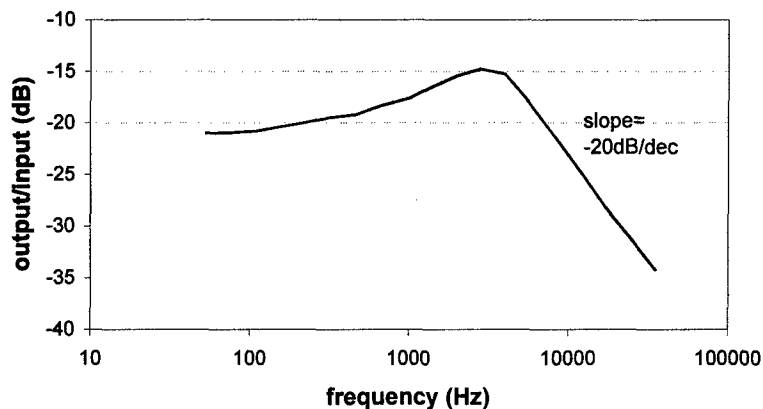
The input-output response of the HWA to dipole amplitude is plotted in Figure 198. The center of the dipole source is positioned 4.5mm away from the HWA, voltage supplied into the shaker is attenuated by the value shown, so the larger the attenuation the lower the applied voltage. The reference value of the attenuation is  $0.7 V_{rms}$  at 40dB. As the applied voltage to the shaker drops, the acceleration of the dipole source decreases linearly. Because the HWA is not directional, we expect the doubling of frequency so the amplitude from the two harmonics at  $1\times$  and  $2\times$  the frequency. The slope of the  $1\times$  harmonic is  $-1$ , like that of the accelerometer. However, for the  $2\times$  harmonic, the output initially falls off at  $-1$ , but falls off at  $-2$  slope at higher attenuation between 50-60dB. Dumbleday attributed this phenomenon to free convection at low signal amplitude[23], but that is not the case here because axis of dipole field is parallel to gravity. Another explanation could be the imperfect symmetry of the polyimide-nickel-polyimide composite forming the hot-wire.

Next, the response of the HWA to changing dipole frequency is examined. The HWA is first calibrated for its thermal frequency response in water. The frequency response of the hot-wire itself is measured by placing the HWA in constant-circuit mode at various overheat. The HWA is placed in a bridge without the feedback, and  $R_1$  is set so that for the bridge to be in balance, the HWA has to reach a particular overheat. The hot-wire  $-3$ dB cutoff frequency near 400Hz. When the HWA operates in the CT mode as shown in Figure 16, the dynamic range extends to 4kHz. This shows that the HWA can respond to the low frequency dipole field in the tens to hundreds of hertz range that aquatic animals commonly encounter.

The response of a single HWA to dipole field is measured by moving the dipole stimulus across the sensor using the setup described in hydrophone experiment[22]. For a single HWA, the TSI anemometer module is used and subsequently amplified by 60dB. The HWA is set to an overheat of 0.1, corresponding to a average temperature increase from ambient of 25°C. The dipole stimulus maintains the same frequency and amplitude while traversing across the sensor and the output of the HWA is sent into an A/D module and the rms voltage of the HWA is measured.



(a)



(b)

**Figure 20:** Frequency response of the HWA in (a) CC mode at various overheat, and (b) CT mode. Both frequency sweep were performed with a sinusoidal disturbance of 200mV and at overheat of 0.05, the hot-wire resistance is 48.2Ω.

The RMS amplitude of the digitized HWA response is plotted in Figure 219, along with the magnitude of calculated pressure gradient. The two curves were shifted so the peak corresponds to right below the dipole source at position zero. The amplitude for both plots was normalized to the maximum value so the peak is at 100% response. The noise level of the HWA sensor was also measured as the dipole traverse across the sensor, but with the minishaker turned off. It is represented by the dotted line, and the amplitude corresponds to about 4% of the peak amplitude.

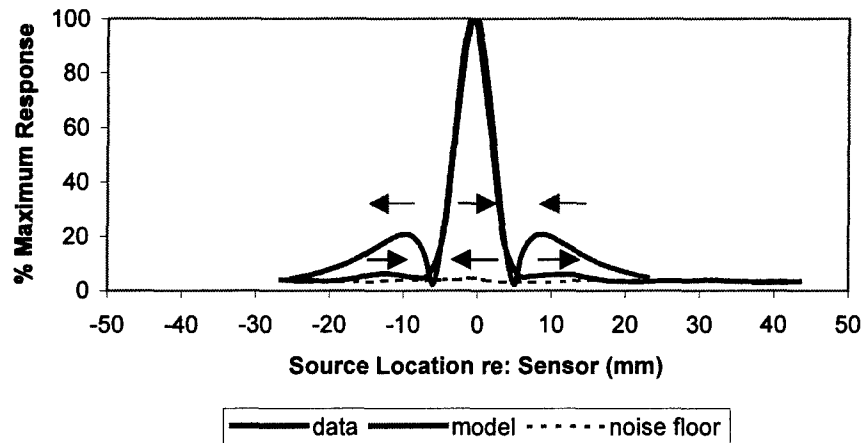


**Figure 21:** Output of the HWA sensor (diamonds) versus the model for pressure gradient in response to changing dipole source location over a range of 72mm. Dipole velocity  $U_0$  is 30cm/s. The output and model value is normalized to the peak of the response (100%), normalized to a particle displacement of  $3\mu\text{m}$ . Flow directions for a given phase (time) of sinusoidal motion differ as a function of source location as shown by arrows of same color. The axis of dipole oscillation is transverse to the HWA and parallel to the direction of dipole position. The dipole frequency is 50Hz, and the HWA is operating with an overheat ratio of 0.12. Dipole is 7.5mm away from the HWA. The dotted line is the noise floor of the HWA, and corresponds to the output of the HWA when the dipole is moved across the sensor, but with the dipole oscillation turned off.

The measured data has good correlation with the model when the sensor is near the dipole source, around where the main peak is located, and far away from the source. However, around 5-20mm from the center where the side lobe should be, which corresponds to a  $180^\circ$  phase shift of the sinusoidal motion, the data from the sensor does not correlate well with the model. One explanation could be the output of the sensor near the side lobe (between 7-20mm away from source) almost overlaps the noise floor, which may completely overlap the side lobes. However, the sensor amplitude at the peak is 20 times the noise floor, and the model prediction shows the side lobe should be at 20% of the amplitude. The model is normalized to a particle displacement of  $3\mu\text{m}$ . The noise floor corresponds to about 4% of that, corresponding to a measurable particle displacement threshold of approximately  $0.1\mu\text{m}$ . This value is similar to the lowest displacement reported by Coombs[24].

Dipole sweep was done in both directions, and the sensor output is the same in each direction. One drawback of using the HWA, as discussed before, is its lack of directionality. Therefore, only the RMS amplitude comparison was performed.

### Array measurement

In the previous experiment, one sensor was used to resolve the dipole field by collecting the data as the dipole source traverse across it. In the real system, it is desirable to simultaneously collect data to locate the dipole source. The artificial lateral line chip with 16 HWA channel is used. An optical micrograph of the packaged array is shown in Figure 22.

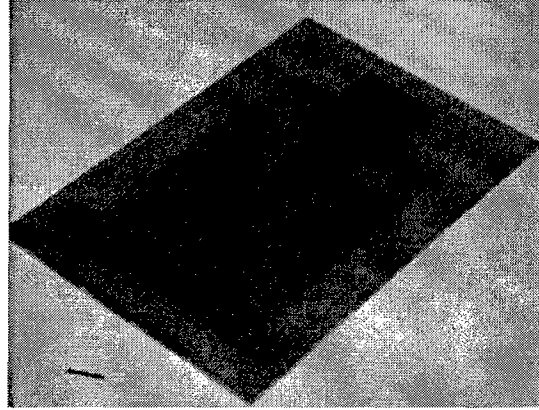


Figure 22: optical photograph of the packaged 16 channel sensor.

The 16-channel HWA array was interfaced with a custom 16-channel constant temperature circuit along with amplifier shown in Figure 164. The bridge ratio in the constant temperature circuit was set to 1, and the amplifier gain to 500. The HWA array used had a  $400\mu\text{m}$  long by  $10\mu\text{m}$  wide hot-wire, with an average resistance of  $42.8\Omega \pm 3\%$  deviation. Overheat of the 16 channel HWA was adjusted using 16 individual potentiometers ( $R_1$ ) to an overheat of 0.06, corresponding to an average  $\Delta T$  of  $15^\circ\text{C}$ . The conservative overheat value used is to prevent the accidental burn-out of any sensor in the array. Typically, HWA used in liquid is limited to an overheat of less than 0.1 due to concerns with bubble-formation that can cause errors in the measurement[25].

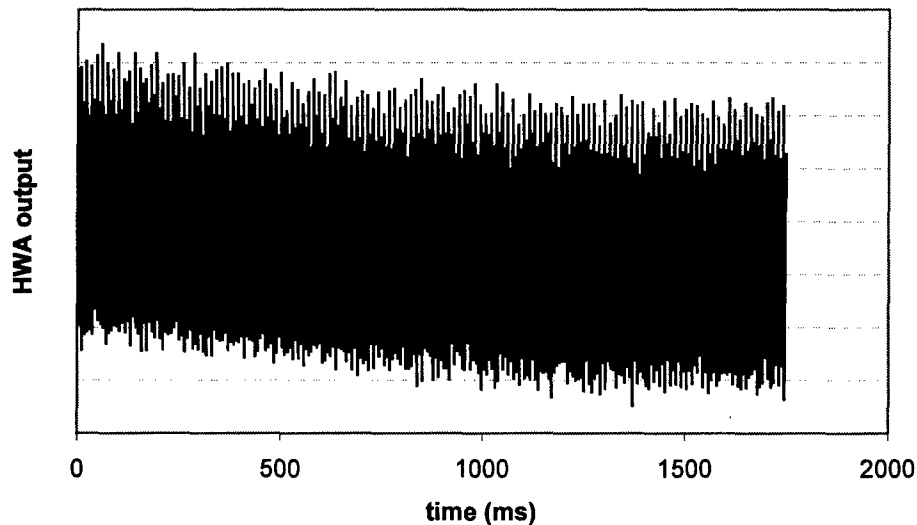
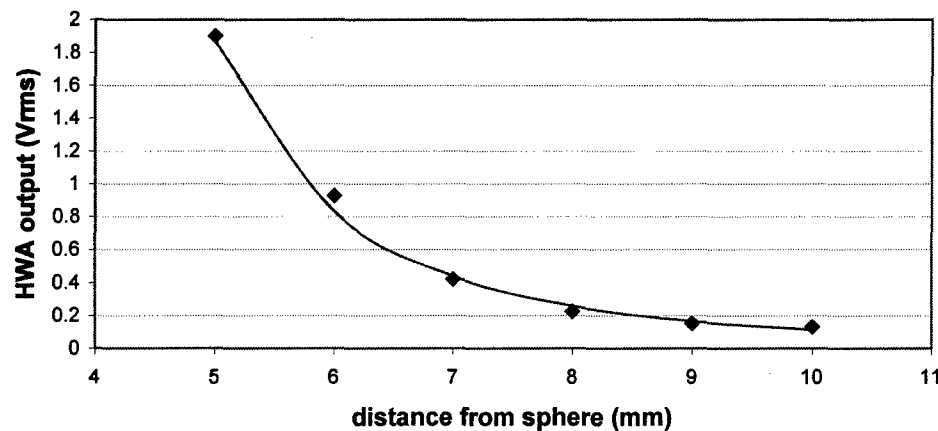


Figure 23: Typical HWA output in response to dipole source. The shaker starts at time  $t=0$ , and it takes approximately 1 min for the DC shift to settle.

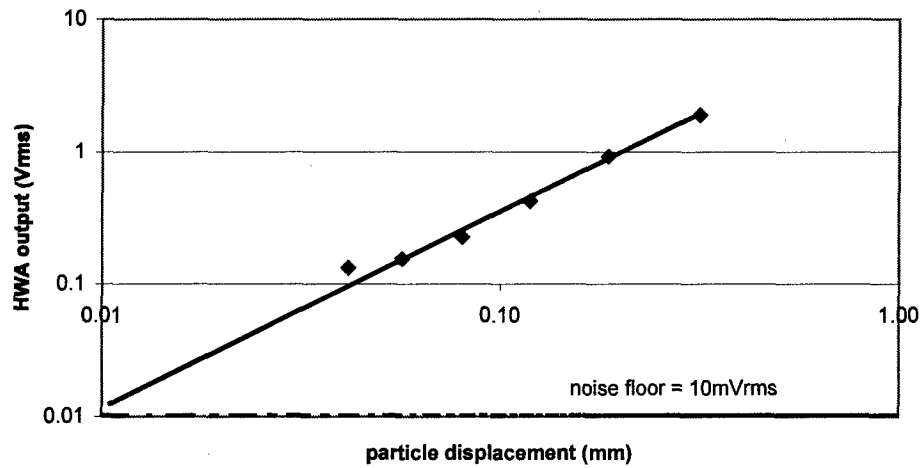
The output of the HWA circuit was sent to a 12-bit 16 channel data acquisition card running LabView. Although a 16 channel sensor array is fabricated and tested, data from only 15 channels are actually collected, the final channel records the waveform from the accelerometer. A typical waveform captured is plotted in Figure 20, with the shaker turned on at  $t=0$ . The waveform shows a slight DC shift occurs for the first second, this transient could be due to some thermal mixing.

To avoid this effect on the measurement, a pause was introduced between the start of the dipole and the start of the data acquisition. The procedure is as follows. First, the motor moves the dipole into position, and then the minishaker starts and creates the dipole field. At the same time a TTL trigger tells the data acquisition software to wait for about 2 seconds, after which data acquisition starts and captures a segment of the overall waveform until approximately 100ms before the minishaker stops. This process is repeated until the dipole source has traversed across the entire range. Each segment of the waveform captured corresponds to a particular sensor channel and dipole location. The composite of the waveform can be compiled together to piece together a spatial response curve.

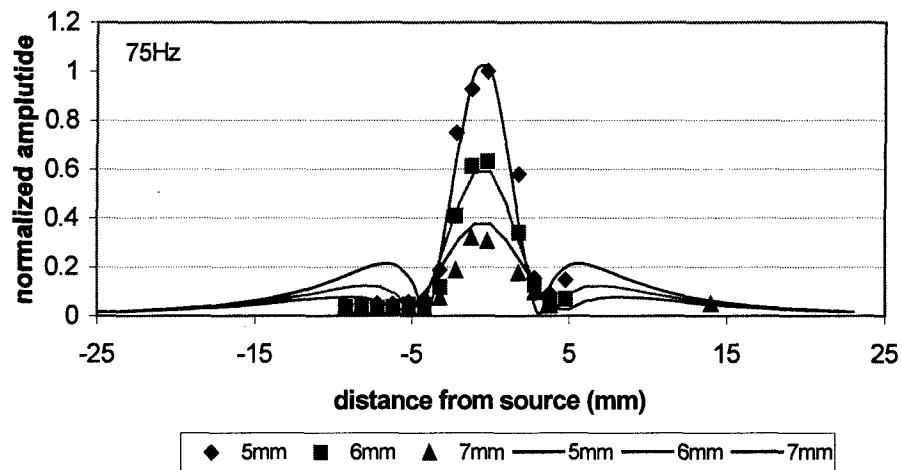


**Figure 24:** Attenuation of the HWA as a function of distance from the source at 50Hz. The data is plotted with the  $1/r^3$  falloff represented with the solid curve-fit line.

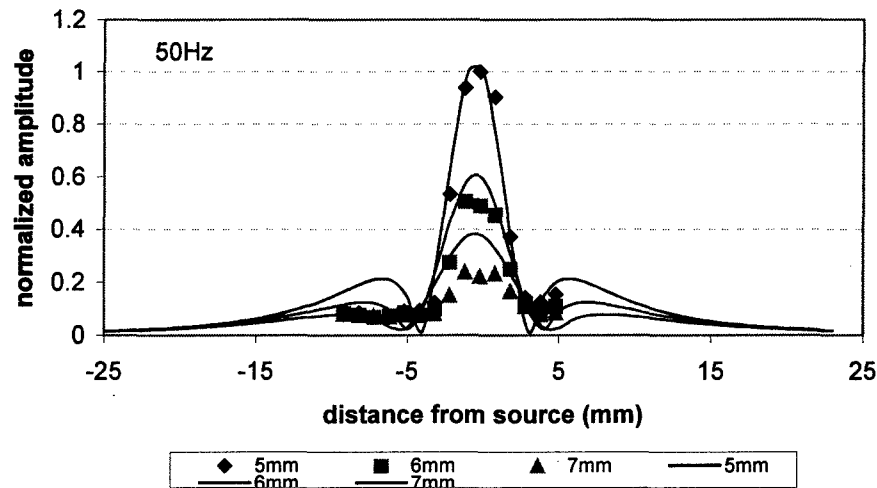
Particle motion that is dominated by near-field dipole flow should fall off very quickly, as a function of  $1/r^3$ , as predicted. The attenuation of the sensor signal to distance from the source is plotted in Figure 23, along with a curve fit line showing that the signal does attenuate at that rate. The same data is also plotted versus the calculated particle displacement based on the time derivative. The dipole velocity  $U_0$  used to calculate the particle displacement is derived from the accelerometer output, and is measured to be around 1m/s with approximately 3mm dipole displacement. The noise floor of the HWA array is measured in absence of any dipole stimulus, and is around  $10\text{mV}_{\text{rms}}$ , as represented by the line. This corresponds to a minimal detectable particle displacement of around  $10\mu\text{m}$ , which is considerably worse than the 100nm threshold measured for the single HWA channel interfacing with a commercial anemometer circuit and amplifier. However, it is cost prohibitive to build such a complicated circuit for all 16 sensor channels.



**Figure 25:** Plot of HWA output versus calculated particle displacement for a dipole source oscillating with  $U_0 = 1\text{m/s}$  and frequency of 50Hz. The noise floor of the HWA array is around  $10\text{ mV}_{\text{rms}}$ , and is shown as the broken line.



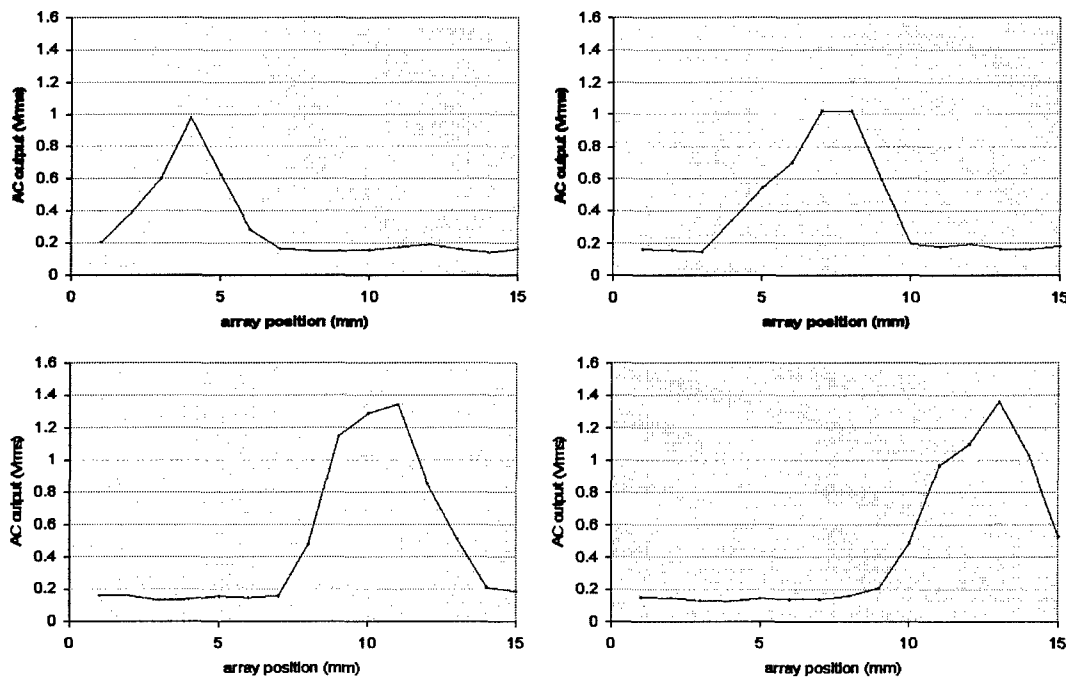




**Figure 26:** Plot of normalized RMS amplitude of the waveform measured using the 16 channel HWA at various dipole height and frequency. The data points from each channel are represented by the symbols. Solid lines represents the model prediction dipole field strength in terms of particle displacement. The amplitude is normalized to the peak when the dipole source is 5mm away from the array.

The RMS amplitude of the 16 channel array is plotted in Figure 265 with the dipole source 5, 6, and 7mm above the array at two different frequencies (50 and 75Hz). The direction of the oscillation is parallel to the axis of the array. As in the single channel response, the HWA data corresponds very well near the peak, but not near the side lobes. Although it is apparent that the side lobe are beginning to form near the right most channel at position 5. The magnitude of the response drops off very quickly, and is also captured by the sensor array.

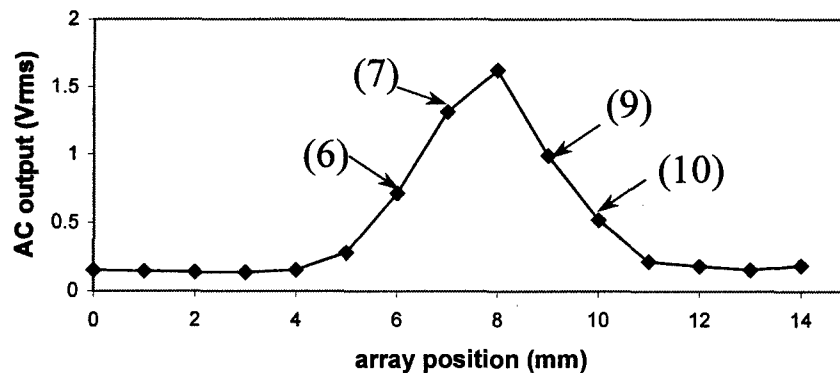
To verify that all 16 channel is working, and also to show the ability of the artificial lateral line sensor array to track the dipole source, the dipole source is traverse along the axis of the sensor array. The output of the HWA array at various dipole source location is plotted in Figure 276, showing that the sensor array can track the motion of the dipole source. The main peak is imaged by the array as it traverse across.



**Figure 27:** Output (Vrms) of the HWA array to various dipole stimulus location. From the upper left clockwise: dipole source above the HWA at 4mm position, 7mm position, 11mm position, and 13mm position.

### HWA directionality

The polyimide-nickel-polyimide hot-film is not completely symmetric. The top polyimide layer is about 20~25% thicker than the bottom polyimide layer due to limitation in curing. This means that after the sensor is actuated, there may be some asymmetry in the temperature profile. The thicker polyimide will face one direction along the axis of the array and reduce the sensitivity, and the thinner layer will face the opposition. This was observed by looking at the ac waveform of the sensor.



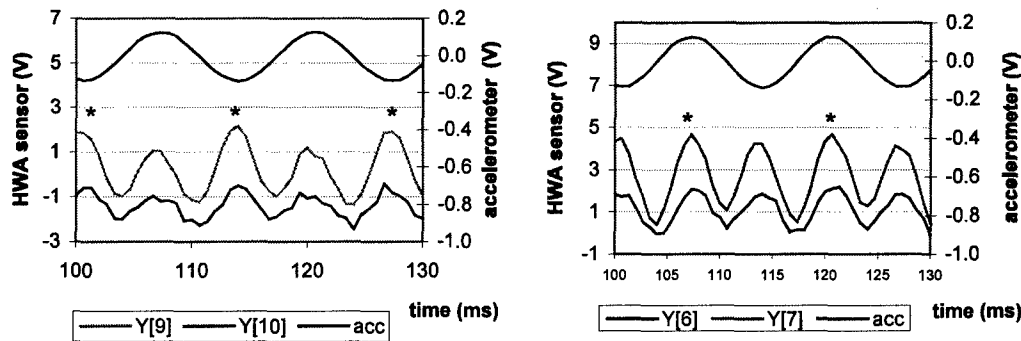


**Figure 28:** The output of the 16 channel HWA in response to a dipole source located at position 8. the dipole is oscillating at 75 Hz frequency with a  $U_0$  of 0.271 m/s. The four channels surrounding the peak are labeled and the waveform compared in the waveform plot, the 2 channel to the left of the dipole position is on a separate plot from the 2 channels to the right of the dipole position, as well as the accelerometer output, whose magnitude is plotted on a separate axis. The frequency doubling characteristic of the HWA output is apparent, with two peaks that corresponds to the minima and maxima of the accelerometer. Of the two peaks in the HWA output, one is slightly larger than the other one and is labeled with an asterisk (\*).

The dipole response from the 16 channel HWA is plotted in Figure 287 when the dipole source is located right above sensor at the 8mm position (position 8). The output of the two sensors to the left of the main peak (6 and 7) is plotted in the waveform on the bottom left, and the output of the two sensors to the right of the main peak (9 and 10) is plotted in the waveform on the bottom right. The frequency doubling characteristics is apparent in the waveform plot because the HWA should be a rectified waveform of particle displacement. For all HWA there exist a waveform peak at both the maxima and the minima of the accelerometer. Because of the thermal asymmetry, the two peaks in the HWA output are not the same. For both set of plots, the larger peak is labeled with an asterisk. For the two sensors to the left of the dipole, the larger peak coincides with the minima of acceleration (maxima of the particle displacement). For the two sensors to the right of the dipole, the larger peak coincides with the maxima of the acceleration. The thicker polyimide layer faces the dipole for one set of sensors, and the thinner layer for the other set of sensors. These partial asymmetries suggest some signal processing algorithm can be used to tell the directionality of the particle displacement.

The output is in phase with the accelerometer and suggesting that the anemometer responds to particle displacement and not velocity, which would be  $90^\circ$  out of phase with the accelerometer signal. The imposed DC flow due to natural convection is estimated to be on the order of 1 mm/s [23], which gives an  $\Omega$  of around 5 according to [23], in the range where the HWA should be displacement sensitive.

#### ***Area 4: New Materials for Bioinspired Sensors***

Traditional MEMS processes are based on silicon materials, which are brittle and cannot sustain large deformation or impact. Biological haircells are made of organic materials that are extremely flexible and yet provide for high sensitivity. In this work, the researchers realized that to achieve high performance of sensors and to reduce the cost of making sensors, new materials are important and should be introduced. A conscious effort was made to incorporate new materials, especially organic materials, and to develop processing methods based on these materials.

Polydimethylsiloxane (PDMS) is the most commonly used elastomer in MEMS, especially microfluidics. Although available in an array of formulations, PDMS's have limited mechanical properties, balanced by good chemical and thermal degradation resistance. In comparison, polyurethanes can be either mechanically softer or stiffer than PDMS, offer better adhesion and tear resistance, and are available in biocompatible formulations that exhibit excellent chemical resistance.

Polyurethane elastomers represent a group of polymers with wide-ranging properties. Polyurethanes have found use in micro-technology as encapsulating structures, chemical sensors [26], electromagnetic absorbers [27], wells for studying blood cells [28], and artificial gecko hairs [29]. In the case of the gecko hairs, polyurethanes were used to mold sub-micron features. Characterization of surface treatment, tensile modulus, thermal degradation, chemical resistance, and adhesive strength has been performed based on two polyurethane rubbers (PMC121 and PMC790 [4]).

#### **Contact Angle Measurement**

Similar to PDMS, the polyurethanes tested exhibit increased contact angle (more hydrophilic) with oxygen plasma treatment (Table 1). Samples were cast and cured according to manufacturer instructions, and then placed in 300W planar oxygen plasma at 500mT for 30 seconds. From the table it is clear that the polyurethanes (+25° on average) do not exhibit the same dramatic change in contact angle as PDMS (+82°). Thus these polyurethanes do not have a clearly defined and thus useful change from hydrophobic to hydrophilic surface character.

**Table 1: Contact angle measurements for DI water on as cast elastomer and elastomer treated for 30s in a 300W O<sub>2</sub> plasma at 500mTorr.**

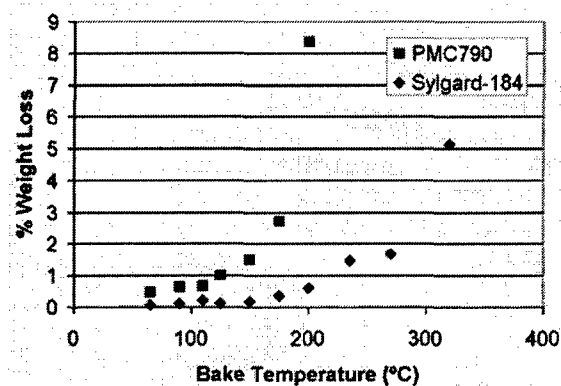
	Sylgard-184	PMC121	PMC790
As cast	88°	119.5°	107°
O <sub>2</sub> Plasma	170°	143°	134°

### Characterization of Mechanical Properties

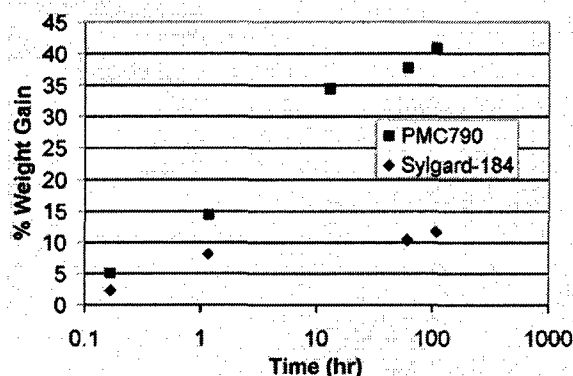
Tensile testing showed that the modulus of PMC121 polyurethane (453 kPa) is similar to that of Sylgard-184 PDMS cured with 10:1 resin to curing agent (750 kPa [30]), while PMC790 polyurethane is an order of magnitude stiffer (19.1 MPa). In addition, the elongation at break of both polyurethanes is well over 200% strain, with PMC121 approaching 500%. Both polyurethanes also exhibit extensive notch-blunting behavior while PDMS readily cracked when deformed. Thus the polyurethanes have low notch-sensitivity and are tougher. Room temperature vulcanizing (RTV) silicones not traditionally used for microfluidic biocompatible systems have been formulated that exhibit lower notch sensitivity as well.

### Thermal Degradation Properties

Thermal degradation testing showed that polyurethanes withstand long-term exposure to temperatures commonly encountered in MEMS processing, with weight loss greater than 1% beginning at 125°C. Sylgard-184 did not exhibit 1% weight loss until 235°C (Figure 29a). Color can be used as an indicator for the thermal degradation of the polyurethanes, beginning with light amber and progressing to a dark orange at temperatures above 200°C.



(a)



(b)

Figure 29: a) Plot of weight % loss versus temperature for PMC790 polyurethane and Sylgard-184 PDMS samples baked for 1 hour. b) Plot of % weight gain of PMC790 and Sylgard-184 samples vs. time soaked in IPA.

## Chemical Resistance

Placing samples of PMC790 polyurethane and Sylgard-184 PDMS in a number of different reagents (see Table 2 and Figure 29b), we found that the polyurethanes exhibit marginal long-term resistance to organic solvents, with good resistance to acids and bases. Chemicals used included DI water, acetone, isopropyl alcohol (IPA), toluene, buffered hydrofluoric acid (10:1) oxide etch (BHF), 2:1 phosphoric acid (HPO<sub>4</sub>), 2:1 hydrochloric acid (HCl), and 40wt% potassium hydroxide (KOH) solution. The PDMS samples exhibited a similar trend, with better resistance to solvents. This data represents the average of three test samples.

**Table 2: Chemical resistance data for PMC790 polyurethane and Sylgard-184 PDMS. Final weight percent change is measured after 24 hour bake at 65°C**

Chemical	PMC790 wt% change		Sylgard-184 wt% change	
	Max	Final	Max	Final
DI Water	2.38	-0.30	-0.15	-0.20
Acetone	71.68	-20.00	6.12	-4.42
IPA	40.90	-25.27	14.09	-4.53
Toluene	148.27	-24.08	70.92	-4.49
BHF	0.53	0.00	-0.09	-0.30
HPO <sub>4</sub>	23.44	14.30	0.05	-0.19
HCl	37.23	-2.66	0.33	-0.22
KOH	1.95	-0.48	-0.65	-0.86

## Adhesion

The post-cure and cast-in-place adhesion of Sylgard-184, PMC121, and PMC790 to various substrates was measured, with and without the addition of a commercial adhesion promoter (Table 3), using 90° peel tests. The stiffer PMC790 exhibited superior adhesion, especially when used with AP134 industrial adhesion promoter. Both polyurethanes showed an order of magnitude greater adhesive strength compared to Sylgard-184 when cast in place.

**Table 3: Adhesion testing. Unless noted, the samples were fully cured before being placed on substrate. Adhesion units are N/100mm, the Newton's of force required to peel a 100mm wide sample.\*The glass carrier broke at the given load before the PMC790 peeled.**

	Sylgard-184	PMC121	PMC790
Sylgard-184	1.0		
PMC121		0.3	
PMC121 w/AP134		0.5	
PMC790			0.6
PMC790 w/AP134			3.9
Glass	2.7	0.2	3.6
Glass w/AP134		2.0	38.6
Silicon	1.0	0.3	1.7
Silicon w/AP134		2.5	43.4
Cast on Glass	2.0	21.3	30.6
Cast on Glass w/AP134		96.9	>100*

## **Molding**

Using techniques developed for casting PDMS microfluidic channels, microfluid channels were cast in PMC121 polyurethane elastomer using a positive photoresist mold (Figure 8). Similar to the Sylgard-184, the PMC121 was able to reproduce micro-scale channels. However, when inlet and outlet ports were punched the PMC121 did not exhibit the tendency to crack that is so problematic with PDMS. The flexibility and ability of the PMC121 to conform and seal to surfaces made it superior to the stiffer PMC790 for microfluidic channels. However, without AP134 or being cast in place, the PMC121 exhibited reduced adhesion to the substrate. Initial tests showed that the PMC121 was able to flow a dyed water solution at low pressure without leakage. The ability of PDMS channels to allow vapor to escape and thus enable deadhead channel filling has not been verified in polyurethane channels.

## **Additional tests**

A number of additional tests were also carried out. Spin casting of the polyurethane elastomers on a traditional photoresist (PR) spinner was not successful. The polyurethanes would coalesce after spinning, creating voids in the resultant film. Oxygen plasma RIE etching was also found to not etch the polyurethanes appreciably. Metal deposition on polyurethanes was successfully performed using both Al and Au. These metals were then patterned via PR patterning and wet etching. Performing PR lithography for lift-off directly on the cured polyurethane was not successful. Upon development, the PR could not be fully patterned, indicating a possible chemical reaction with the polyurethane or an optical effect causing incomplete exposure of the bottom PR layer. These tests utilized AZ 5214 EIR, and other PR's may be more compatible.

## Summary and Conclusions

The work conducted in the past three and half years have met the project goals in all objective areas and exceeded the expectations in some. Most significant achievement in this effort has been:

- The successful development of three generations of artificial haircells and characterization of performances;
- The development of haircell sensors whose hairs can be bent by more than 90 degrees without fracture;
- The successful implementation of arrayed flow sensors on integrated circuit substrates with signal processing capabilities;
- The successful characterization of the artificial haircell sensors and match of performance to modeling;
- The discovery and implementation of new, functional materials for the MEMS field and microfabrication in general;
- The direct comparison of performance of biological haircells and artificial haircells in flow imaging of simple events (dipole movement).

This effort paves the way for future development of prototype sensors of larger scale. Certain industrial applications of the sensor arrays have become immediately possible, such as low cost bidirectional flow sensors for HVAC system monitoring.

The results that have been obtained so far clearly point to the fact that haircells with sophisticated functions and much improved robustness can be made and successfully used by the air force.



### **Personnel Supported**

- 1) Jack Chen, Graduate Student, Electrical and Computer Engineering Department. Jack Chen successfully defended his Ph.D. thesis in January of 2005.
- 2) Jonathan Engel, Graduate Student, Mechanical and Industrial Engineering Department
- 3) Jun Zou, Graduate Student and then Postdoctoral Research Associated (2002), Electrical and Computer Engineering Department
- 4) Zhi Fan, Senior Research Associate, Electrical and Computer Engineering Department

## Publications

Z. Fan, J. Chen, C. Liu, "Development of artificial lateral line sensors", IEEE workshop on solid state sensors and actuators, 2000, Hilton Head, SC.

J. Li, Z. Fan, J. Chen, J. Zou, C. Liu, F. Delcomyn, "High yield microfabrication process for biomimetic artificial haircell sensors", Smart Electronics, MEMS, and Nanotechnology Conference (Conference 4700), SPIE's 9th Annual International Symposium on Smart Structures and Materials, 17-21 March 2002, San Diego, CA.

Jun Zou, Ph.D. thesis, "Micro Electro Mechanical Systems for Radio Frequency Applications" 2002.

Zhifang Fan, Jack Chen, Jun Zou, David Bullen, Chang Liu, and Fred Delcomyn, "Design and Fabrication of Artificial Lateral-Line Flow Sensors", J. Micromechanics and Microengineering, Vol. 12, No. 5, pp. 655-661, September 2002.

C. Liu, J. Zou, J. Chen, Z. Fan, and Fred Delcomyn, "Plastic Deformation Magnetic Assembly Method and Its Applications," 7th Symposium on Magnetic Materials, Processes and Devices, 202nd Electrochemical Society Meeting, Salt Lake City, UT, Oct 20-25, 2002.

C. Liu, J. Chen, J. Zou, and Z. Fan, "Three Dimensional PDMA Assembly: Design, Process and Applications," The MEMS Symposium, 2002 International Mechanical Engineering Congress (IMECE 2002), New Orleans, LA, Nov. 17-22, 2002.

J. Chen, J. Zou, and C. Liu, "A Micromachined, Out-of-Plane Anemometer," Proceedings of IEEE Int. Conf. MEMS, (MEMS 02), Las Vegas, NV, 2002.

J. Chen, Z. Fan, J. Zou, J. Engel, and C. Liu, "Two Dimensional Micromachined Flow Sensor Array for Fluid Mechanics Studies," ASCE Journal of Aerospace Engineering, Vol. 16, No. 2, pp. 85-97, 2003.

J. Chen, J. Engel, and C. Liu, "Development of Polymer Based Artificial Haircell using Surface Micromachining and 3D Assembly," Int. Conf. On Solid-state Sensors and Actuators, June 2003.

J. Engel, J. Chen, and C. Liu, "Development of Polyimide Flexible Tactile Sensor Skin," Journal of Micromechanics and Microengineering, vol. 13, pp. 359-366, 2003.

J. Chen and C. Liu, "Development and Characterization of Surface Micromachined, Out-Of-Plane Hot-Wire Anemometer," IEEE/ASME Journal of Microelectromechanical Systems (JMEMS), vol. 12, pp. 979-988, 2003

Z. Fan, J. M. Engel, J. Chen, and C. Liu, "Parylene Surface-Micromachined Membranes for Sensor Applications," Microelectromechanical Systems, Journal of, vol. 13, pp. 484-490, 2004

E. Goluch, K. Shaikh, K. Ryu, J. Chen, J. Engel, and C. Liu, "A microfluidic method for sensor fabrication on curved surfaces," presented at The American Institute of Chemical Engineers (AIChE) 2004 Annual Meeting, Austin, TX, 2004.

J. Engel, Z. Fan, L. Zhao, J. Chen, and C. Liu, "Smart brick - A low cost, modular wireless sensor for civil structure monitoring," presented at International Conference on Computing, Communications and Control Technologies (CCCT 2004), Austin, TX, 2004.

J. Chen, Z. Fan, J. Engel, and C. Liu, "Towards Modular Integrated Sensors: The Development of Artificial Haircell Sensors Using Efficient Fabrication Methods," presented at IEEE/RSJ International Conference on Intelligent Robots and Systems, Las Vegas, NV, 2003.

J. Engel, J. Chen, X. Wang, Z. Fan, C. Liu, and D. Jones, "Technology Development of Integrated Multi-modal and Flexible Tactile Skin for Robotics Applications," presented at IEEE/RSJ International Conference on Intelligent Robots and Systems, Las Vegas, NV, 2003.

C. Liu, J. Chen, J. Engel, J. Zou, X. Wang, Z. Fan, K. Ryu, K. Shaikh, and D. Bullen, "Polymer micromachining and applications in sensors, microfluidics, and nanotechnology," presented at 226th National Meeting of the American Chemical Society, New York, NY, 2003

J. Engel, J. Chen, and C. Liu, "Polymer-Based MEMS Multi-Modal Sensory Array," presented at 226th National Meeting of the American Chemical Society (ACS), New York, NY, 2003

C. Liu, J. Chen, J. Engel, and Z. Fan, "Biomimetic micro sensors based on polymer micromachining," presented at American Chemical Society National Meeting, Anaheim, CA, 2004

#### **New Discoveries, inventions, or patent disclosures**

C. Liu and J. Zou, "A vertical micro inductor and the fabrication process for such", US patent approved (UIUC file number: TF00111), 2003.

C. Liu, W. Sutomo and D. Bullen, "A Low Cost Sensor for In-Situ Monitoring of Parylene Deposition Thickness", US patent pending.

C. Liu and J. Chen, "Micromachined, Arrayable Hot-wire Anemometers and Fabrication Process for Same", US patent pending.

#### **Honors/Awards**

2002 - Jack Chen won IEEE Electron Devices Society Distinguished Graduate Student Fellowship (one out of five in the world)

2003 - Jonathan Engel won a Motorola Graduate Assistantship from Motorola Corporation.

2004 - Chang Liu won the University Of Illinois College Of Engineering Xerox Award for Faculty Research; Chang Liu was elected to the University of Illinois Center for Advanced Studies as a Research Associate.

## References

- [1] J. Chen and C. Liu, "Development and characterization of surface micromachined, out-of-plane hot-wire anemometer," *Journal of Microelectromechanical Systems*, vol. 12, pp. 979-88, 2003.
- [2] K. Ryu and C. Liu, "Methods for precision patterning of PDMS thin film and applications," *IEEE/ASME Journal of Microelectromechanical Systems (JMEMS)*, vol. in print, 2004.
- [3] K. Shida and J. I. Yuji, "Discrimination of Material Property by Pressure-Conductive Rubber Sheet Sensor with Multi-sensing Function," presented at IEEE International Symposium on Industrial Electronics, 1996.
- [4] *Smooth-On, Inc.* [www.smooth-on.com](http://www.smooth-on.com).
- [5] F. Jiang, Y.-C. Tai, C.-M. Ho, R. Karan, and M. Garstenauer, "Theoretical and experimental studies of micromachined hot-wire anemometers," presented at Proceedings of 1994 IEEE International Electron Devices Meeting, 11-14 Dec. 1994, San Francisco, CA, USA, 1994.
- [6] T. Ebefors, E. Kalvesten, and G. Stemme, "Three dimensional silicon triple hot-wire anemometer based on polyimide joints," presented at IEEE MEMS, New York, 1998.
- [7] T. Neda, K. Nakamura, and T. Takumi, "A polysilicon flow sensor for gas flow meters," *Sensors & Actuators*, vol. A54, pp. 621-631, 1996.
- [8] S. Dijkgraaf, "A short personal review of the history of lateral line research," in *The Mechanosensory lateral line : neurobiology and evolution*, H. Mèunz, Ed. New York: Springer-Verlag, 1989, pp. 7-14.
- [9] S. Dijkgraaf, "The functioning and significance of the lateral-line organs," *Biology Review*, vol. 38, pp. 51-105, 1962.
- [10] A. J. Kalmijn, "Functional Evolution of Lateral Line and Inner Ear Sensory Systems," in *The Mechanosensory lateral line : neurobiology and evolution*, H. Mèunz, Ed. New York: Springer-Verlag, 1989, pp. 187-215.
- [11] S. Coombs, P. Gèorner, and H. Mèunz, *The Mechanosensory lateral line : neurobiology and evolution*. New York: Springer-Verlag, 1989.
- [12] S. Coombs and J. C. Montgomery, "Enigmatic Lateral Line System," in *Comparative hearing. Fish and amphibians*, A. N. Popper, Ed. New York: Springer, 1999, pp. xviii, 438 p.
- [13] S. Coombs, "Smart skins: Information processing by lateral line flow sensors," *Autonomous Robots*, vol. 11, pp. 255-261, 2001.
- [14] S. M. van Netten and A. B. A. BKroese, "Dynamic behavior and micromechanical properties of the cupula," in *The Mechanosensory lateral line : neurobiology and evolution*, H. Mèunz, Ed. New York: Springer-Verlag, 1989, pp. 247-263.
- [15] E. J. Denton and J. A. B. Gray, "Some observation on the forces acting on neuromasts in fish lateral line canals," in *The Mechanosensory lateral line : neurobiology and evolution*, H. Mèunz, Ed. New York: Springer-Verlag, 1989, pp. 229-245.
- [16] A. J. Hudspeth, "The cellular basis of hearing: the biophysics of hair cells," *Science*, vol. 230, pp. 745-52, 1985.
- [17] A. J. Hudspeth and V. S. Markin, "The ear's gears: mechanoelectrical transduction by hair cells," *Physics Today*, vol. 47, pp. 22-8, 1994.

- [18] A. B. A. Kroese and S. M. Vannetten, "The Application of Incident Light Polarization Microscopy for the Visualization of Vertebrate Sensory Hair-Cells Invivo," *Journal of Microscopy-Oxford*, vol. 145, pp. 309-317, 1987.
- [19] M. J. Madou, *Fundamentals of microfabrication : the science of miniaturization*, 2nd ed. Boca Raton, Fla.: CRC Press, 2002.
- [20] G. T. A. Kovacs, *Micromachined transducers sourcebook*. Boston, Ma.: Wcb, 1998.
- [21] J. Chen, J. Engel, M. Chang, and C. Liu, "3D out-of-plane flow sensor array with integrated circuits," presented at Eurosensors XVI, Rome, 2004.
- [22] S. Coombs, M. Hastings, and J. Finneran, "Modelling and measuring lateral line excitation patterns to changing dipole source locations," *Journal of Comparative Physiology A Sensory Neural and Behavioral Physiology*, vol. 178, pp. 359-371, 1996.
- [23] P. S. Dobbelday, "Hot-film anemometry measurement of hydroacoustic particle motion," *Journal of the Acoustical Society of America*, vol. 79, pp. 2060-6, 1986.
- [24] S. Coombs, R. R. Fay, and J. Janssen, "Hot-film anemometry for measuring lateral line stimuli," *Journal of the Acoustical Society of America*, vol. 85, pp. 2185-93, 1989.
- [25] H. H. Bruun, *Hot-wire anemometry : principles and signal analysis*. Oxford ; New York: Oxford University Press, 1995.
- [26] A. Bratov, J. Munoz, C. Dominguez, and J. Bartoli, "Photocurable polymers applied as encapsulating materials for ISFET production," *Sensors and Actuators B*, vol. 25, pp. 823-825, 1995.
- [27] T. Soh and O. Hashimoto, "Absorption characteristics in 50-110 GHz of 60 GHz wave absorber using epoxy-modified urethane rubber mized with carbon particles," presented at Terahertz and Gigahertz Electronics and Photonics II, San Diego, CA, 2000.
- [28] J.-U. Meyer and M. Biehl, "Micropatterned biocompatible materials with applications for cell cultivation," *Journal of Micromechanics and Microengineering*, vol. 5, pp. 172-174, 1995.
- [29] D. Campolo, S. Jones, and R. S. Fearing, "Fabrication of gecko foot-hair like nano structures and adhesion to random rough surfaces," presented at IEEE Conference on Nanotechnology, 2003.
- [30] D. Armani and C. Liu, "Re-configurable fluid circuits by PDMS elastomer micromachining," presented at IEEE International Conference on MEMS, Orlando, FL, 1999.